Nanoscale

PAPER

View Article Online
View Journal | View Issue

Cite this: *Nanoscale*, 2025, **17**, 26194

Nucleation and crystallization of metal oxides from carbonates

Yingying Jiang,[a,b] Guoming Lin[a,b] and Utkur Mirsaidov *[a,b,c,d]

Received 15th April 2025,
Accepted 30th September 2025

DOI: 10.1039/d5nr01525a

rsc.li/nanoscale

Metal oxides play an important role in catalysis, integrated circuit fabrication, and optical coatings. A common approach for obtaining these oxides is the thermal decomposition of solid precursor templates, among which metal carbonates are the most widely used ones. Despite the importance of the process, the atomic-scale mechanisms governing the transformation of such templates into oxides remain insufficiently understood. Using *in situ* transmission electron microscopy (TEM), we show that $La_2(CO_3)_3{\cdot}8H_2O$ and $Ce_2(CO_3)_3{\cdot}8H_2O$ undergo a multistep transformation: (i) dehydrogenation, (ii) decarbonization, and (iii) crystallization. Our observations reveal concurrent compositional and structural changes within the precursor templates during their conversion to oxides. These findings offer valuable insights into the crystallization of metal oxides, providing a basis for optimizing their properties for diverse technological applications.

Introduction

Metal oxides such as CeO_2,[1,2] La_2O_3,[3,4] ZnO,[5,6] and Al_2O_3 [7] are widely used in catalysis,[1,5,7] electronics,[3] and optics,[4] due to their exceptional properties, including catalytic activity,[1,5] ionic conductivity,[2] high dielectric constant (k),[3] and ultraviolet (UV) absorption.[6] For instance, CeO_2 is a key component in automotive catalytic converters and solid oxide fuel cells,[1,2] while La_2O_3 is used as a high-k dielectric material in the manufacturing of integrated circuits.[3] A major strategy for producing metal oxide nanostructures (*e.g.*, particles,[8–10] plates,[11,12] and films[13]) is the thermal decomposition of solid or wet-coated precursor templates, such as metal (oxy)carbonates[8,9,12] and hydroxides.[10,11,14] This method enables precise control over the morphology,[8,9] composition,[11] and properties[9,11] of the resulting metal oxides.

The transformation process typically involves phase changes, often progressing through intermediate metastable phases, accompanied by the release of volatile byproducts, such as CO_2 and H_2O.[11,12,14] During this transformation, the crystallization of the oxide phase determines the crystal grain size,[12,15] composition,[11] and defect characteristics,[16] which in turn influence the electronic,[17] catalytic,[11,16] optical,[18] and mechanical[15] properties of the oxides.

Despite the widespread use of thermal decomposition for oxide synthesis, many details about the atomic-scale transformation remain unknown. This knowledge gap arises primarily from the lack of methods capable of directly probing the process. While previous studies based on macroscopic characterization methods, such as X-ray diffraction (XRD),[19–22] Fourier transform infrared spectroscopy (FTIR),[22,23] and thermogravimetric analysis (TGA),[22,23] have provided important insights into the transformations, they lack the resolution to capture atomic-scale nucleation pathways driving crystallization in real time. Transmission electron microscopy, although capable of atomic resolution, is conventionally performed under vacuum at room temperature, requiring sample cooling and transfer that interrupt ongoing reactions.[8,10,14,24] These constraints hinder the observation of rapid, short-lived events occurring on the timescale of seconds, leaving the early stages of structural evolution largely inaccessible.

Here, we employed *in situ* TEM imaging with atomic-scale resolution[20,25–29] to directly monitor the real-time transformation of metal carbonates into polycrystalline oxide nanostructures. This approach enables the simultaneous tracking of nucleation and phase evolution under controlled heating and gas environments, offering mechanistic insights that are beyond the reach of conventional methods. To investigate both intrinsic and environment-driven transformation processes, we used two types of metal carbonate templates: $La_2(CO_3)_3{\cdot}8H_2O$ and $Ce_2(CO_3)_3{\cdot}8H_2O$. In the former, decomposition proceeds intrinsically to La_2O_3, with lanthanum retaining its +3 oxidation state, whereas in the latter, decomposition

[a]*Department of Physics, National University of Singapore, Singapore, 117551, Singapore. E-mail: mirsaidov@nus.edu.sg*
[b]*Centre for BioImaging Sciences, Department of Biological Sciences, National University of Singapore, Singapore, 117557, Singapore*
[c]*Centre for Advanced 2D Materials and Graphene Research Centre, National University of Singapore, Singapore, 117546, Singapore*
[d]*Department of Materials Science and Engineering, National University of Singapore, Singapore, 117575, Singapore*

is oxygen-driven, leading to the formation of CeO_2, accompanied by the oxidation of cerium from Ce^{3+} to Ce^{4+}.

Results and discussion

The as-synthesized $La_2(CO_3)_3{\cdot}8H_2O$ template is a plate-like crystal (Fig. 1A: $t - t_0 = 0$ s). It has a layered structure with an interlayer spacing of 8.6 Å (Fig. 1A and S1). Each basic layer consists of lanthanum polyhedra, in which La^{3+} ions are coordinated with CO_3^{2-} ions and water molecules. Approximately 75% of the total water molecules are coordinated within the polyhedra, while the remaining water molecules reside in the interlayer regions. Upon heating from 23 to 800 °C at a rate of 10 °C min^{-1}, the single-crystalline template decreased in size and transformed into polycrystalline La_2O_3 (Fig. 1A: $t - t_0$ = 4700 s). Similarly, when the $Ce_2(CO_3)_3{\cdot}8H_2O$ template was annealed under an oxygen atmosphere (760 Torr of 20% O_2 and 80% Ar) instead of a vacuum, it transformed into CeO_2 (Fig. 1B and S5), in a manner analogous to the transformation of $La_2(CO_3)_3{\cdot}8H_2O$ into La_2O_3.

To elucidate the transformation mechanisms of these carbonates into their respective oxides, we tracked their evolution in real time. We first investigated the structural changes

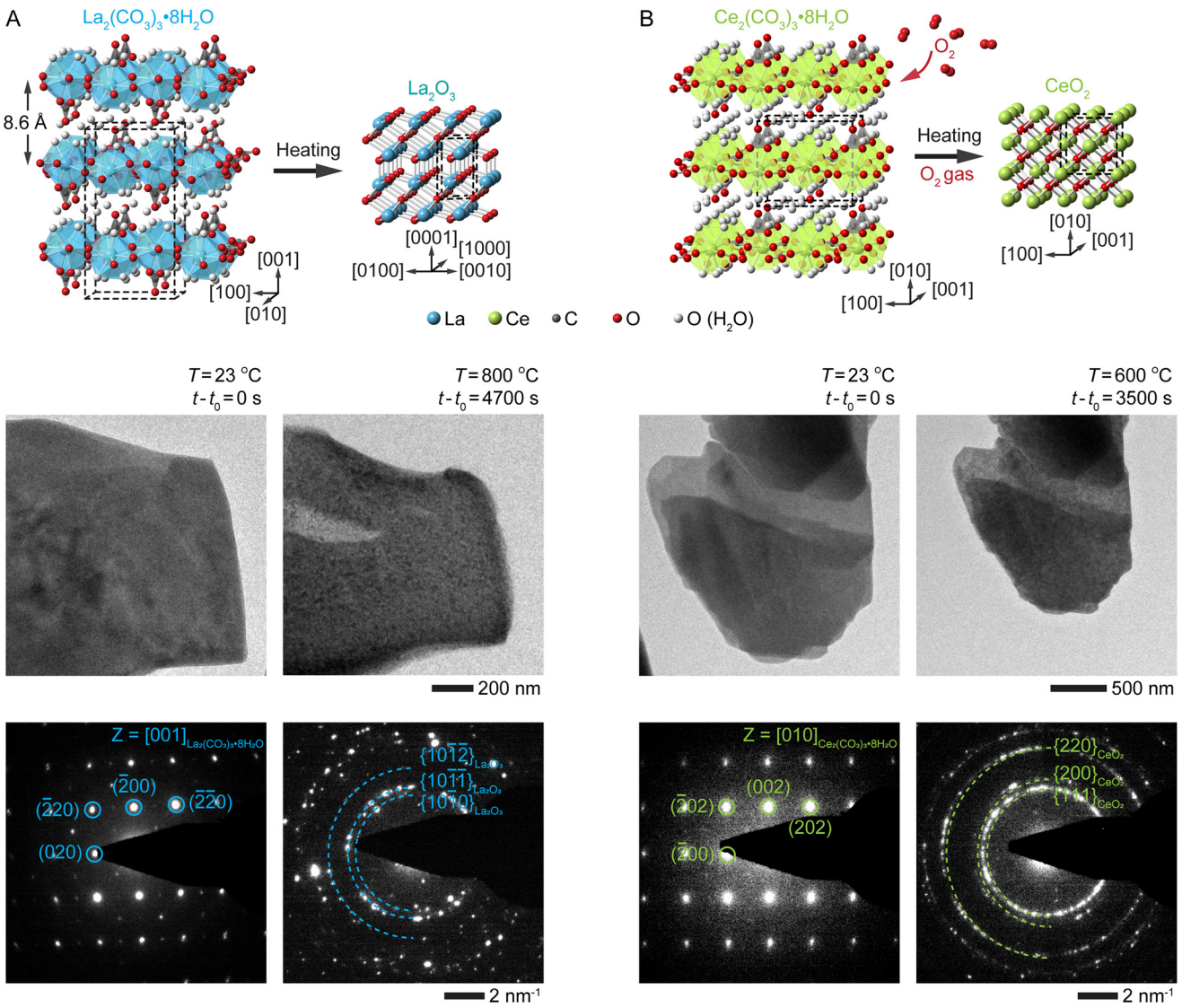

Fig. 1 Transformations of carbonate templates into metal oxides. Schematics[12,30–32] and *in situ* TEM images with the corresponding electron diffraction patterns showing the transformation of single-crystalline (A) $La_2(CO_3)_3{\cdot}8H_2O$ and (B) $Ce_2(CO_3)_3{\cdot}8H_2O$ templates into polycrystalline La_2O_3 and CeO_2 plates, respectively, during heating. The $La_2(CO_3)_3{\cdot}8H_2O$ template was heated from 23 to 800 °C at a rate of 10 °C min^{-1} in a vacuum, while the $Ce_2(CO_3)_3{\cdot}8H_2O$ template was heated from 23 to 600 °C at the same rate under an oxygen atmosphere (760 Torr of 20% O_2 and 80% Ar). For clarity, H atoms in H_2O molecules are omitted in the schematics. Black dashed rectangular prisms indicate the corresponding unit cells. t_0 is the time point at which we started increasing the temperature.

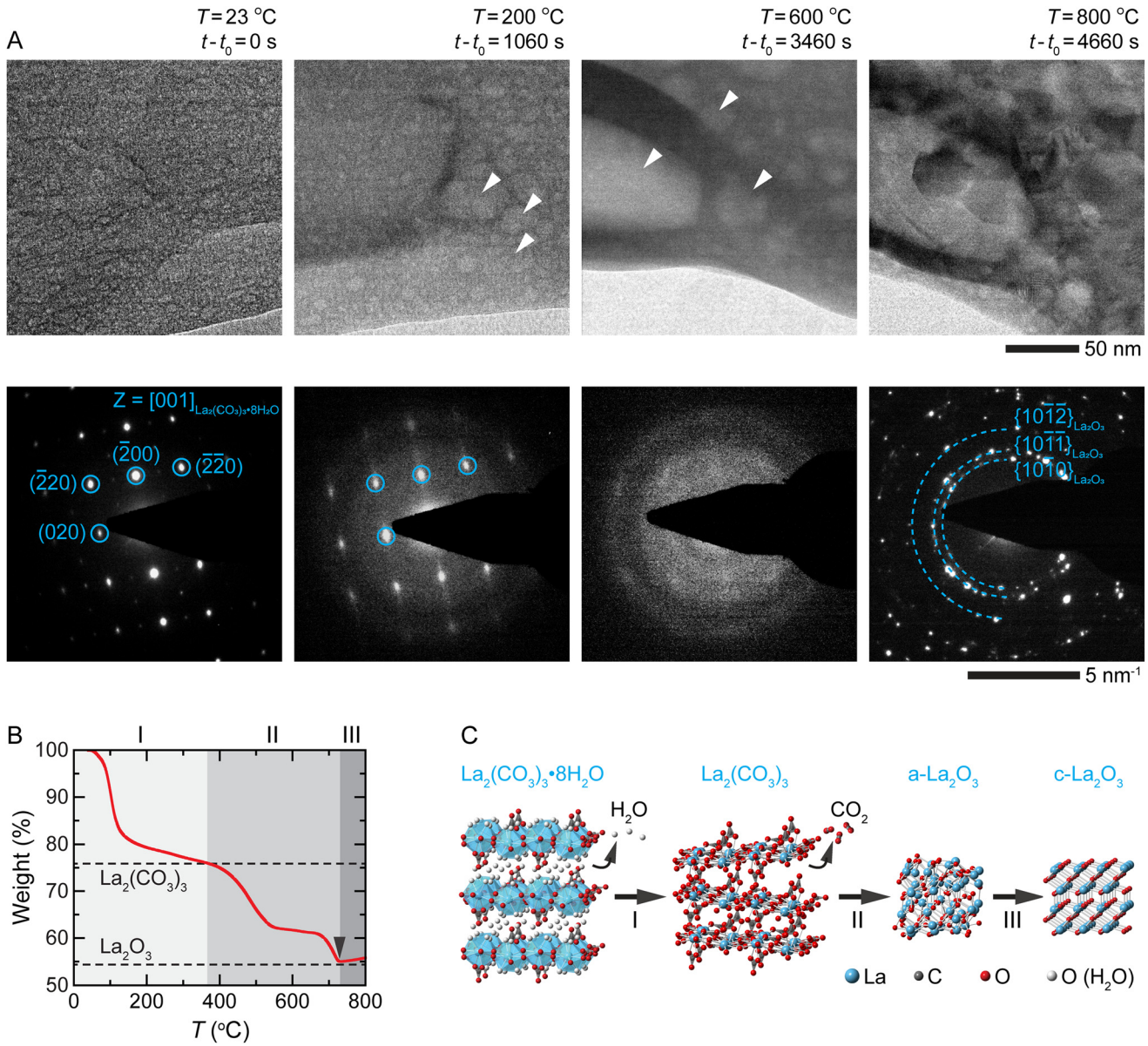

Fig. 2 Transformation pathway of the $La_2(CO_3)_3{\cdot}8H_2O$ template into La_2O_3. (A) TEM image series and the corresponding electron diffraction patterns of a $La_2(CO_3)_3{\cdot}8H_2O$ template transforming into La_2O_3 upon heating from 23 to 800 °C at a rate of 10 °C min^{-1} in a vacuum. (B) TGA profile of $La_2(CO_3)_3{\cdot}8H_2O$ heated from 40 to 800 °C at a rate of 10 °C min^{-1} in air. (C) Schematic diagram showing the transformation stages: $La_2(CO_3)_3{\cdot}8H_2O$ undergoes dehydrogenation into $La_2(CO_3)_3$ (step I), decarbonization into a-La_2O_3 (step II), and subsequent crystallization (step III). White arrows in (A) at $t - t_0$ = 1060–3460 s indicate the small voids that form within the template. The black arrow in (B) indicates the temperature at which the template composition approaches that of a stoichiometric La_2O_3. The dashed horizontal lines in (B) correspond to the theoretical weight percentages of $La_2(CO_3)_3$ and La_2O_3 derived from the decomposition of $La_2(CO_3)_3{\cdot}8H_2O$. t_0 is the time point at which we started increasing the temperature.

during the transformation of $La_2(CO_3)_3{\cdot}8H_2O$ as the temperature was increased from 23 to 800 °C under vacuum (Fig. 2A). With increasing temperature, the template gradually lost its crystallinity and became amorphous (Fig. 2A: $t - t_0$ = 0–3460 s), followed by recrystallization of this amorphous phase into a polycrystalline La_2O_3 phase (Fig. 2A: $t - t_0$ = 4660 s). The TGA profile of the template revealed two primary stages of weight loss (Fig. 2B): dehydrogenation occurring between 40 and 370 °C, and decarbonization occurring between 370 and 730 °C. These processes can be described by the following reactions:

$$La_2(CO_3)_3 \cdot 8H_2O \rightarrow La_2(CO_3)_3 + 8H_2O \quad (1)$$

$$La_2(CO_3)_3 \rightarrow La_2O_3 + 3CO_2 \quad (2)$$

Fig. 2C summarizes the transformation pathway. During the initial heating stage, most of the water molecules are removed from the template (I: dehydrogenation step), resulting

in the loss of its crystallinity. In the subsequent stage, the CO_3^{2-} ions in $La_2(CO_3)_3$ decompose to form amorphous La_2O_3 (a-La_2O_3) and CO_2(g) (II: decarbonization step). Finally, the a-La_2O_3 undergoes crystallization into polycrystalline oxide (c-La_2O_3) (III: crystallization step). As shown in Fig. 2C, the interlayer and coordinated water molecules are released below 370 °C, indicating their minimal contribution to decarbonization and crystallization. In contrast, carbonate decomposition governs the evolution of $La_2(CO_3)_3$ into La_2O_3, thereby impacting its crystallinity, grain size, and defect density.[33,34] Note that the observed transformation pathway is independent of the heating rate; similar transformations were observed when $La_2(CO_3)_3{\cdot}8H_2O$ templates were heated at 25 and 100 °C min^{-1} instead of 10 °C min^{-1} (Fig. S2 and S3 *vs.* Fig. 2A).

To better visualize the crystallization of a-La_2O_3, we imaged the process at higher magnification, as shown in Fig. 3. When a-La_2O_3 was heated from 600 to 900 °C at a rate of 30 °C min^{-1} (Fig. 3A), small La_2O_3 nuclei with sizes of 1–3 nm began to form at the edge of the template at 671 °C (Fig. 3B: $t - t_0$ = 142 s). Note that this temperature is significantly lower than the 730 °C required for the template composition to reach stoichiometric La_2O_3, as shown in Fig. 2B. This crystallization process is thermodynamically driven by the reduction in free energy,[35,36] while the plate-like template promotes heterogeneous nucleation by lowering the critical energy barrier through its large surface area and high-energy edge sites.[37] Upon further heating, these nuclei grew into larger grains and came into contact with adjacent grains, producing polycrystalline La_2O_3 (Fig. 3B: $t - t_0$ = 206–448 s).

While $La_2(CO_3)_3{\cdot}8H_2O$ transforms into La_2O_3 without chemical interaction with the surrounding gaseous environment (eqn (1) and (2)), the thermal decomposition of other template materials can yield non-stoichiometric oxides. For example, in contrast to annealing in air, annealing $Ce_2(CO_3)_3{\cdot}8H_2O$ either under vacuum or N_2 produces oxygen-deficient CeO_{2-x}, in which cerium exists in both Ce^{4+} and Ce^{3+} oxidation states (Fig. S6 and S7). Hence, it is important to consider the effect of the atmosphere on the thermal decomposition process. To address this, we investigated the evolution of the $Ce_2(CO_3)_3{\cdot}8H_2O$ template during thermal decomposition under an oxygen atmosphere.

Our *in situ* TEM observations show that the transformation pathway of $Ce_2(CO_3)_3{\cdot}8H_2O$ closely resembles that of $La_2(CO_3)_3{\cdot}8H_2O$, with both undergoing an amorphous intermediate phase before crystallizing into the respective metal oxides (Fig. 4A). The TGA profile of $Ce_2(CO_3)_3{\cdot}8H_2O$ exhibited two distinct weight-loss steps during this process (Fig. 4B).

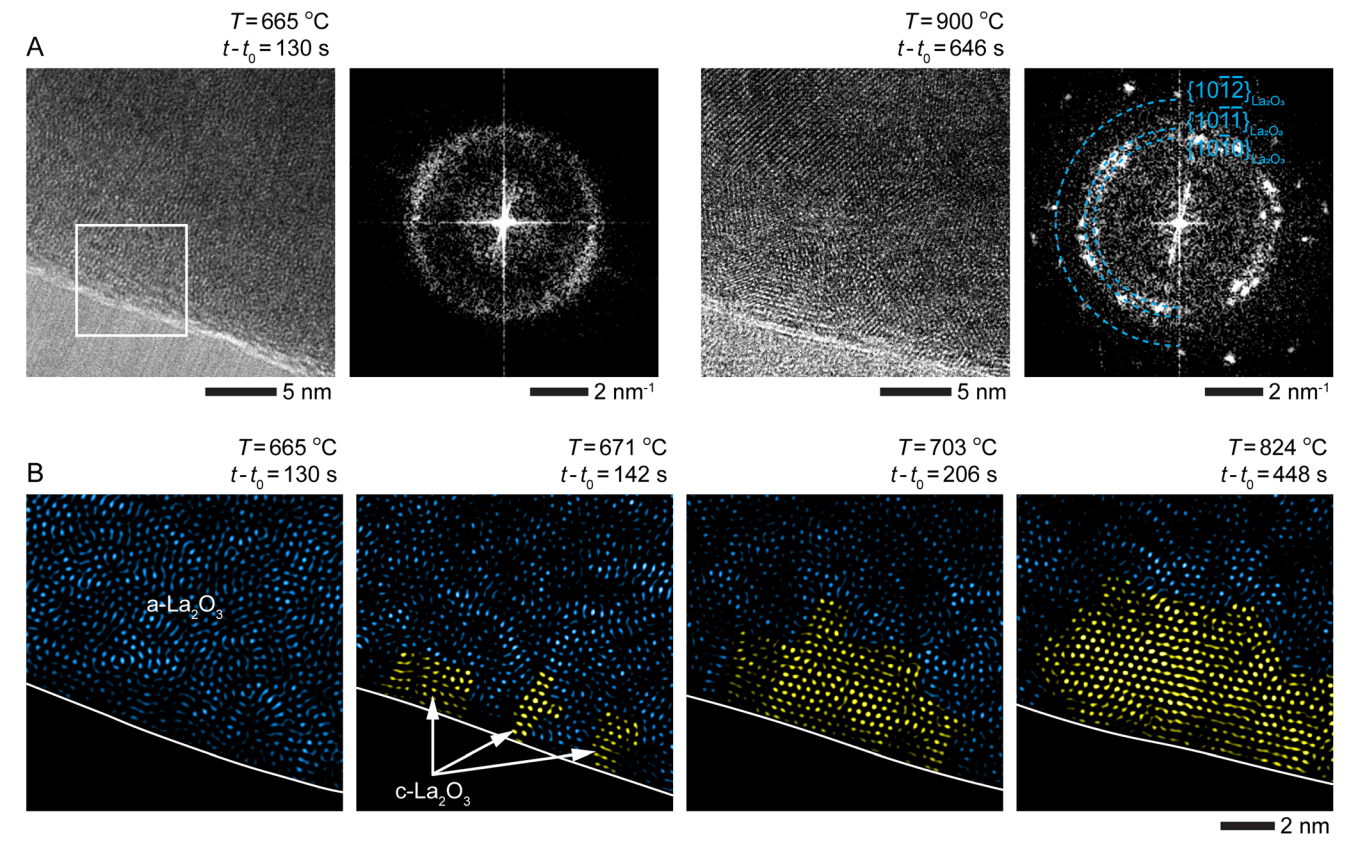

Fig. 3 Nucleation of La_2O_3 nanocrystals in the amorphous film. (A) TEM and the corresponding FFT images showing the crystallization of the amorphous film into the polycrystalline La_2O_3 upon heating from 600 to 900 °C at a rate of 30 °C min^{-1} in a vacuum (SI Video S1). (B) Sequence of inverse FFT images of the area (white box) in (A) showing the nucleation ($t - t_0$ = 130–142 s) and growth ($t - t_0$ = 206–448 s) of La_2O_3 nanocrystals (see Fig. S4 for the unprocessed TEM and FFT images). The amorphous and crystalline regions are false-colored in blue and yellow, respectively. t_0 is the time point at which we started increasing the temperature.

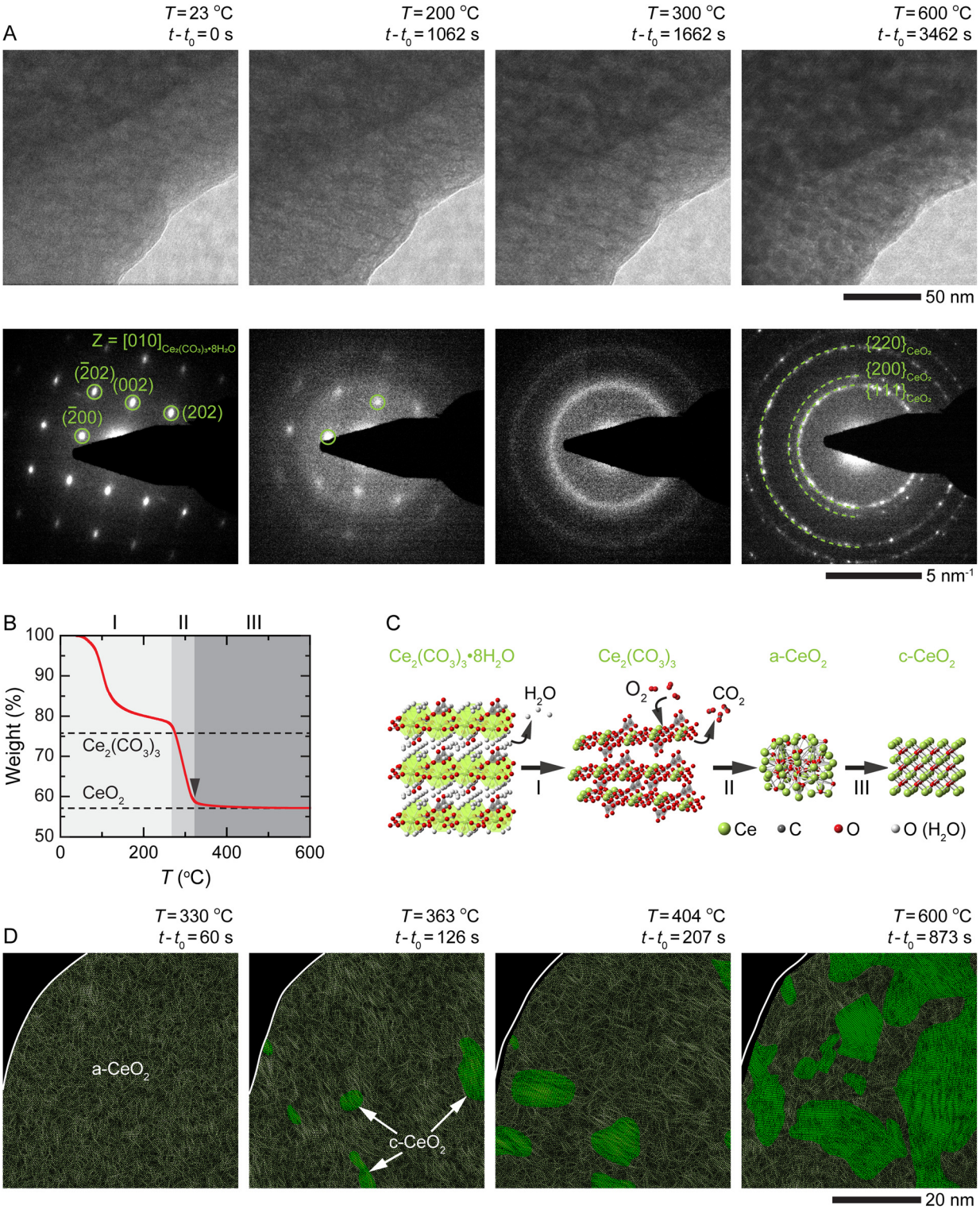

Fig. 4 Transformation pathway of the $Ce_2(CO_3)_3{\cdot}8H_2O$ template into CeO_2. (A) TEM image series and the corresponding electron diffraction patterns of the $Ce_2(CO_3)_3{\cdot}8H_2O$ template transforming into CeO_2 upon heating from 23 to 600 °C at a rate of 10 °C min^{-1} in O_2 (760 Torr of 20% O_2 and 80% Ar). (B) TGA profile of $Ce_2(CO_3)_3{\cdot}8H_2O$ heated from 40 to 600 °C at a rate of 10 °C min^{-1} in air. (C) Schematic diagram showing the transformation stages: $Ce_2(CO_3)_3{\cdot}8H_2O$ undergoes dehydrogenation into $Ce_2(CO_3)_3$ (step I), oxidation and decarbonization into a-CeO_2 (step II), and subsequent crystallization (step III). (D) Sequence of inverse FFT images showing the nucleation ($t - t_0$ = 60–126 s) and growth ($t - t_0$ = 207–873 s) of CeO_2 nanocrystals (see Fig. S8 for the unprocessed TEM and FFT images) upon heating from 300 to 600 °C at a rate of 30 °C min^{-1} in O_2 (SI Video S2). The amorphous and crystalline regions are false-colored in brown and green, respectively. The black arrow in (B) indicates the temperature at which the template composition approaches that of a stoichiometric CeO_2. The dashed horizontal lines correspond to the theoretical weight percentages of $Ce_2(CO_3)_3$ and CeO_2 derived from the decomposition of $Ce_2(CO_3)_3{\cdot}8H_2O$. t_0 is the time point at which we started increasing the temperature.

First, $Ce_2(CO_3)_3{\cdot}8H_2O$ underwent dehydrogenation to form $Ce_2(CO_3)_3$ at 40–270 °C. This was then followed by oxidative decarbonization of $Ce_2(CO_3)_3$ into CeO_2 at 270–330 °C, described by the following reactions:[12]

$$Ce_2(CO_3)_3 \cdot 8H_2O \rightarrow Ce_2(CO_3)_3 + 8H_2O \quad (3)$$

$$Ce_2(CO_3)_3 + \frac{1}{2}O_2 \rightarrow 2CeO_2 + 3CO_2 \quad (4)$$

At 330 °C, the composition of the template closely approached stoichiometric CeO_2 (Fig. 4B), which enabled the nucleation of CeO_2 nanocrystals within the amorphous phase (Fig. 4D).

Comparison of the atmosphere-dependent structural evolution of $Ce_2(CO_3)_3{\cdot}8H_2O$ and $La_2(CO_3)_3{\cdot}8H_2O$ templates reveals that O_2 significantly accelerates the transformation of $Ce_2(CO_3)_3{\cdot}8H_2O$, but not $La_2(CO_3)_3{\cdot}8H_2O$. At 300 °C, the $Ce_2(CO_3)_3{\cdot}8H_2O$ template retained its crystalline structure under vacuum (Fig. S6A: $t - t_0$ = 1660 s), but lost crystallinity under an oxygen atmosphere (Fig. 4A: $t - t_0$ = 1662 s). This behavior is consistent with oxidative decarbonization of $Ce_2(CO_3)_3{\cdot}8H_2O$ occurring at a much lower temperature (270–330 °C) compared to the non-oxidative decarbonization of $La_2(CO_3)_3$ (370–730 °C) (Fig. 4B and 2B).

This difference can be attributed to the greater positive charge density of Ce^{4+}, which has a higher charge (+4) and a smaller ionic radius (0.87 Å) than those of La^{3+} (+3, 1.03 Å) and Ce^{3+} (+3, 1.01 Å).[38] The higher polarizing power of Ce^{4+} induces a stronger distortion of the CO_3^{2-} electron cloud, weakening its C–O bonds and thereby facilitating decomposition at substantially lower temperatures than in the cases of La^{3+} and Ce^{3+}.

To further support this explanation, we calculated the CO_2 desorption energy (ΔE) as a proxy for the decarbonization step during the transformation of metal carbonates into oxides. Specifically, ΔE was evaluated for $La_2O_2CO_3$, $Ce_2O_2CO_3$, and $Ce_2O_3CO_3$, corresponding to CO_2 release from oxycarbonate intermediates containing La^{3+}, Ce^{3+}, and Ce^{4+}, respectively. For example, $La_2O_2CO_3$ decomposes as $La_2O_2CO_3 \rightarrow La_2O_3 + CO_2$. The calculated ΔE for the Ce^{4+}-containing intermediate ($Ce_2O_3CO_3$) is significantly lower (101.4 eV) than that for the La^{3+}- and Ce^{3+}-containing intermediates (223.3 eV for $La_2O_2CO_3$ and 193.9 eV for $Ce_2O_2CO_3$) (Fig. S9).

Note that this carbonate-to-oxide transformation approach can be extended to other rare-earth systems. For example, Fig. S10 shows that $Y_2(CO_3)_3{\cdot}2H_2O$ transforms into Y_2O_3 and $Pr_2(CO_3)_3{\cdot}8H_2O$ transforms into Pr_6O_{11}. Taken together, these results suggest that, for rare-earth carbonates whose thermal decomposition does not involve changes in the metal oxidation states, the gaseous atmosphere under which these carbonates are annealed has little to no impact on their transformation to metal oxides.[12,39,40] By contrast, when oxidation to higher valence states is required, the presence of O_2 facilitates oxidation and accelerates the overall conversion process, whereas the lack of oxygen results in oxygen-deficient oxides with coexisting mixed-valence metal states.

Conclusions

Our *in situ* TEM studies reveal that the transformation of metal carbonate templates into metal oxides proceeds through a sequence of three distinct steps: dehydrogenation of the carbonate, followed by decarbonization into an amorphous metal oxide, and finally crystallization of the oxide. These results underscore the significance of real-time tracking in revealing transient structural states during crystallization, thereby providing mechanistic insights that can guide the controlled synthesis and optimization of oxide materials for a wide range of applications.

Methods

Materials

The following reagents from Sigma-Aldrich Co. (St Louis, MO, USA) were used to synthesize the $La_2(CO_3)_3{\cdot}8H_2O$ and $Ce_2(CO_3)_3{\cdot}8H_2O$ templates: lanthanum(III) nitrate hexahydrate ($La(NO_3)_3{\cdot}6H_2O$, cat. no. 203548), cerium(III) nitrate hexahydrate ($Ce(NO_3)_3{\cdot}6H_2O$, cat. no. 238538), sodium bicarbonate ($NaHCO_3$, cat. no. S6297), and ethylene glycol (EG, cat. no. 324558). Yttrium(III) nitrate hexahydrate ($Y(NO_3)_3{\cdot}6H_2O$, cat. no. Y820618, Shanghai Macklin Biochemical Co., Ltd., Shanghai, China) and praseodymium(III) nitrate hexahydrate ($Pr(NO_3)_3{\cdot}6H_2O$, cat. no. P106054, Shanghai Aladdin Biochemical Technology Co., Ltd., Shanghai, China) were used to synthesize the $Y_2(CO_3)_3{\cdot}2H_2O$ and $Pr_2(CO_3)_3{\cdot}8H_2O$ templates, respectively. Deionized (DI) water with a resistivity of 18.2 MΩ cm was used to prepare all aqueous solutions in this study.

Synthesis of carbonate templates

The $La_2(CO_3)_3{\cdot}8H_2O$ templates were synthesized based on a modified procedure of Yin *et al.*[12] Specifically, 0.23 g of $NaHCO_3$, 2 mL of EG, and 7 mL of DI water were mixed in a 50 mL centrifuge tube. Next, 0.44 g of $La(NO_3)_3{\cdot}6H_2O$ was dissolved in 3 mL of DI water, and the solution was added to the centrifuge tube. The resulting mixed solution was maintained at ambient temperature for 6 h. The precipitate was collected by centrifugation, washed five times with DI water, and dried overnight at 60 °C.

The $Ce_2(CO_3)_3{\cdot}8H_2O$, $Y_2(CO_3)_3{\cdot}2H_2O$, and $Pr_2(CO_3)_3{\cdot}8H_2O$ templates were synthesized following the same procedures as the $La_2(CO_3)_3{\cdot}8H_2O$ templates, but instead of $La(NO_3)_3{\cdot}6H_2O$, 0.44 g of $Ce(NO_3)_3{\cdot}6H_2O$, $Y(NO_3)_3{\cdot}6H_2O$, or $Pr(NO_3)_3{\cdot}6H_2O$ was used, respectively. Additionally, for $Ce_2(CO_3)_3{\cdot}8H_2O$, the template solution was maintained at ambient temperature for 3 h rather than 6 h.

In situ TEM experiments

A Titan S/TEM (Thermo Fisher Scientific Ltd., Hillsboro, OR, USA) operated at an accelerating voltage of 300 kV was used for *in situ* TEM studies. Image series were acquired at 5 frames per second using a Gatan K2 IS camera (Gatan Inc., Pleasanton, CA, USA), with an electron flux ranging from 100 to 200 e^- $Å^{-2}$ s^{-1}.

DENSsolutions Wildfire and Climate TEM holders (DENSsolutions, Delft, Netherlands) were used for *in situ* heating studies of the templates in a vacuum and in a gaseous environment (20% O_2 and 80% Ar at 1 atm pressure), respectively. The gas mixture (O_2 + Ar) was flowed into the TEM holder at a flow rate of 40–50 μL min^{-1} using the DENSsolutions gas delivery system.

Schematics of crystal structures

The crystal structures of the carbonate templates and the crystallized oxides shown in Fig. 1A and B were adapted from ref. 12, 30–32 and rendered using the CrystalMaker® 9.0.3 software package.[41] The LaO_{10}, CeO_{12} and CO_3 polyhedra are depicted in translucent blue, green, and grey, respectively.

Electron diffraction profiles

The radial diffraction profiles in Fig. S6B are the plots of the summed intensity $S(k)$ obtained from electron diffraction images after background subtraction. The summed intensity was calculated using the following equation:

$$S(k) = \sum I(\mathbf{k}) \tag{5}$$

Here, $\mathbf{k} = (k_x,k_y)$ and $k = \sqrt{k_x^2 + k_y^2}$ are the outward radial vector from the center of the diffraction pattern and its corresponding length, and $I(\mathbf{k})$ is the diffraction intensity at that point.

Thermal decomposition in a tube furnace

Thermal decomposition of the templates was carried out in a tube furnace (NBD-O1200-50IT-80F, Henan Nobody Materials Science and Technology Co., Zhengzhou, China) under either air or an N_2 environment. For each study, 100–200 mg of a template was placed in a quartz boat, which was then positioned at the center of a quartz tube with an inner diameter of 42 mm. For decomposition in air, the samples were heated from room temperature to 800 °C at a rate of 10 °C min^{-1} under static air. For decomposition under N_2, the tube was pumped down and purged with pure N_2 three times prior to heating. The samples were then heated from room temperature to 800 °C at the same rate under a continuous N_2 flow of approximately 200 sccm, sufficient to create a slight overpressure relative to the ambient atmosphere.

XRD, TGA, and XPS characterization

The XRD patterns shown in Fig. S1 and S5 were obtained using a Bruker D8 Advance Powder X-ray Diffractometer (Bruker, Billerica, MA, USA) with a 2θ range of 5°–70° and a step size of 0.02° s^{-1}. The XRD patterns shown in Fig. S10 were obtained using a PANalytical X'Pert PRO Powder X-ray Diffractometer (Malvern Panalytical, Almelo, The Netherlands) with a 2θ range of 5°–80° and a step size of 0.02° s^{-1}.

The TGA profiles displayed in Fig. 2B and 4B were acquired using a Discovery TGA (TA Instruments, New Castle, DE, USA). During TGA measurements, the samples were heated in air from 40 to 600 or 800 °C at a rate of 10 °C min^{-1}.

The XPS results shown in Fig. S7 were obtained using a Kratos Axis Ultra DLD spectrometer (Kratos Analytical, Shimadzu, Japan), equipped with a monochromatized Al Kα X-ray source (15 kV, 3 mA, beam size 300 × 700 μm^2). The pass energy was set to 40 eV for the high-resolution scans. Raw XPS data were calibrated using the binding energy of the C 1s peak at 284.8 eV, and background subtraction was performed using the Shirley method.[42] Data analysis was performed with XPSPEAK 4.1 software.[43] The Ce 3d spectra were deconvoluted into Ce^{3+} and Ce^{4+} components. The fractions of Ce^{3+} ($f_{Ce^{3+}}$) and Ce^{4+} ($f_{Ce^{4+}}$) shown in Fig. S7A were calculated using the following equations:[44]

$$A_{Ce^{3+}} = A_{v'} + A_{u'} \tag{6}$$

$$A_{Ce^{4+}} = A_v + A_{v''} + A_{v'''} + A_u + A_{u''} + A_{u'''} \tag{7}$$

$$f_{Ce^{3+}} = \frac{A_{Ce^{3+}}}{A_{Ce^{3+}} + A_{Ce^{4+}}} \tag{8}$$

$$f_{Ce^{4+}} = \frac{A_{Ce^{4+}}}{A_{Ce^{3+}} + A_{Ce^{4+}}} \tag{9}$$

Here, $A_{v'}$ and $A_{u'}$ represent the deconvoluted peak areas at binding energies of 885.2 and 903.1 eV, respectively, corresponding to Ce^{3+} contribution. The Ce^{4+} contribution is given by the peak areas A_v, $A_{v''}$, $A_{v'''}$, A_u, $A_{u''}$, and $A_{u'''}$ associated with binding energies of 882.4 (v), 888.8 (v″), 898.0 (v‴), 900.7 (u), 907.3 (u″), and 916.6 eV (u‴), respectively.

Computational methods

All calculations displayed in Fig. S9 were performed using the Gaussian 09 software package.[45] The B3LYP hybrid density functional theory (DFT) method[46,47] was used in combination with the CEP-31G basis set,[48–50] which includes effective core potentials for rare-earth elements such as cerium and lanthanum. The charge and spin multiplicity were assigned according to the expected oxidation states of the metal centers. Single-point energy calculations were performed on optimized geometries of nanoscale clusters to refine the electronic energy values. This computational setup provides a reliable balance between accuracy and efficiency for systems containing f-block elements.[51]

The geometric structures of oxide clusters (La_2O_3, Ce_2O_3, and CeO_2), their corresponding oxycarbonate intermediates ($La_2O_2CO_3$, $Ce_2O_2CO_3$, and $Ce_2O_3CO_3$), and CO_2 were fully optimized without symmetry constraints. Vibrational frequency analyses were performed, and the absence of imaginary frequencies confirmed that these structures correspond to optimized geometries located at stable local minima on the potential energy surface, rather than transition states or saddle points.

The CO_2 desorption energy (ΔE) from oxycarbonate intermediates was calculated as a proxy for the decarbonization step of metal carbonates using:

$$\Delta E = E_{oxide} + E_{CO_2} - E_{oxycarbonate} \tag{10}$$

Here, E_{oxide}, E_{CO_2}, and $E_{oxycarbonate}$ are the total energies of the isolated oxide cluster, the CO_2 molecule, and the oxycarbonate intermediate, respectively.

Author contributions

Y. J. and U. M. conceived the study. Y. J. conducted the experiments and analyzed the data. G. L. performed the DFT simulations. Y. J. and U. M. wrote the manuscript.

Conflicts of interest

There are no conflicts to declare.

Data availability

The data supporting this article have been included as part of the supplementary information (SI). Supplementary information is available. See DOI: https://doi.org/10.1039/d5nr01525a.

Acknowledgements

This work was supported by the Singapore National Research Foundation's Competitive Research Program funding (NRF-CRP23-2019-0001) and the Ministry of Education-Singapore (MOE-T2EP10220-0003).

References

1 T. Montini, M. Melchionna, M. Monai and P. Fornasiero, *Chem. Rev.*, 2016, **116**, 5987–6041.
2 T. Mori, J. Drennan, J.-H. Lee, J.-G. Li and T. Ikegami, *Solid State Ionics*, 2002, **154–155**, 461–466.
3 K. Xiong and J. Robertson, *Appl. Phys. Lett.*, 2009, **95**, 022903.
4 S. B. Brachetti-Sibaja, S. E. Rodil, M. A. Domínguez-Crespo, A. M. Torres-Huerta, E. Rodríguez and A. B. López-Oyama, *Thin Solid Films*, 2017, **636**, 615–621.
5 A. Wang, W. Quan, H. Zhang, H. Li and S. Yang, *RSC Adv.*, 2021, **11**, 20465–20478.
6 H. Wang, W. Lin, X. Qiu, F. Fu, R. Zhong, W. Liu and D. Yang, *ACS Sustainable Chem. Eng.*, 2018, **6**, 3696–3705.
7 R. Prins, *J. Catal.*, 2020, **392**, 336–346.
8 S. K. Meher and G. R. Rao, *J. Colloid Interface Sci.*, 2012, **373**, 46–56.
9 L. Xu, Z. Li, Q. Cai, H. Wang, H. Gao, W. Lv and J. Liu, *CrystEngComm*, 2010, **12**, 2166–2172.
10 L. Zhu, S. Pu, K. Liu, T. Zhu, F. Lu and J. Li, *Mater. Lett.*, 2012, **83**, 73–75.
11 T. Ye, W. Huang, L. Zeng, M. Li and J. Shi, *Appl. Catal., B*, 2017, **210**, 141–148.
12 S. Yin, Y. Minamidate, S. Tonouchi, T. Goto, Q. Dong, H. Yamane and T. Sato, *RSC Adv.*, 2012, **2**, 5976–5982.
13 I. Bretos, R. Jiménez, J. Ricote and M. L. Calzada, *Chem. Soc. Rev.*, 2018, **47**, 291–308.
14 Q. Mu and Y. Wang, *J. Alloys Compd.*, 2011, **509**, 396–401.
15 R. Kavitha, S. R. Hegde and V. Jayaram, *Mater. Sci. Eng., A*, 2003, **359**, 18–23.
16 M. Hu, W. Yang, H. Tan, L. Jin, L. Zhang, P. Kerns, Y. Dang, S. Dissanayake, S. Schaefer, B. Liu, *et al.*, *Matter*, 2020, **2**, 1244–1259.
17 N. W. Kwak and W. Jung, *Acta Mater.*, 2016, **108**, 271–278.
18 E. A. Villegas, C. M. Aldao, R. Savu, L. A. Ramajo and R. Parra, *Phys. Status Solidi A*, 2018, **215**, 1800107.
19 T. Arii, A. Kishi, M. Ogawa and Y. Sawada, *Anal. Sci.*, 2001, **17**, 875–880.
20 R. Warringham, S. Mitchell, R. Murty, R. Schäublin, P. Crivelli, J. Kenvin and J. Pérez-Ramírez, *Chem. Mater.*, 2017, **29**, 4052–4062.
21 C. Vaysse, L. Guerlou-Demourgues and C. Delmas, *Inorg. Chem.*, 2002, **41**, 6905–6913.
22 J. Pérez-Ramírez, G. Mul, F. Kapteijn and J. A. Moulijn, *J. Mater. Chem.*, 2001, **11**, 821–830.
23 J. Pérez-Ramırez, G. Mul and J. A. Moulijn, *Vib. Spectrosc.*, 2001, **27**, 75–88.
24 Y. Zhao, X. Jia, G. Chen, L. Shang, G. I. Waterhouse, L.-Z. Wu, C.-H. Tung, D. O'Hare and T. Zhang, *J. Am. Chem. Soc.*, 2016, **138**, 6517–6524.
25 Y. Jiang, M. Duchamp, S. J. Ang, H. Yan, T. L. Tan and U. Mirsaidov, *Nat. Commun.*, 2023, **14**, 104.
26 Y. Jiang, Z. M. Wong, H. Yan, T. L. Tan and U. Mirsaidov, *ACS Nano*, 2025, **19**, 3886–3894.
27 T. Ghosh, J. M. Arce-Ramos, W.-Q. Li, H. Yan, S. W. Chee, A. Genest and U. Mirsaidov, *Nat. Commun.*, 2022, **13**, 6176.
28 S. W. Chee, J. M. Arce-Ramos, W. Li, A. Genest and U. Mirsaidov, *Nat. Commun.*, 2020, **11**, 2133.
29 Y. Jiang, A. M. H. Lim, H. Yan, H. C. Zeng and U. Mirsaidov, *Adv. Sci.*, 2023, **10**, 2302663.
30 D. B. Shinn and H. A. Eick, *Inorg. Chem.*, 1968, **7**, 1340–1345.
31 R. Sarbajna, A. S. Devi, K. Purandhar and M. V. Suryanarayana, *Int. J. ChemTech Res.*, 2013, **5**, 2810–2820.
32 S. N. Kabekkodu, A. Dosen and T. N. Blanton, *Powder Diffr.*, 2024, **39**, 47–59.
33 L. Zeng, D. B. Buchholz, D. T. Keane, T. J. Marks, J. E. Medvedeva and M. J. Bedzyk, *Chem. Mater.*, 2024, **36**, 5965–5975.
34 Y. Wang, H. Wang, C. S. Li, J. Q. Feng, L. H. Jin, Z. M. Yu, P. Odier and P. X. Zhang, *Ceram. Int.*, 2015, **41**, 14270–14275.
35 C. Yang, Y. Hirose, S. Nakao, N. L. H. Hoang and T. Hasegawa, *Appl. Phys. Lett.*, 2012, **101**, 052101.
36 J. L. M. Rupp, C. Solenthaler, P. Gasser, U. P. Muecke and L. J. Gauckler, *Acta Mater.*, 2007, **55**, 3505–3512.
37 N. Karpukhina, R. G. Hill and R. V. Law, *Chem. Soc. Rev.*, 2014, **43**, 2174–2186.
38 R. D. Shannon, *Acta Crystallogr., Sect. A*, 1976, **32**, 751–767.
39 L. Paama, I. Pitkänen, H. Halttunen and P. Perämäki, *Thermochim. Acta*, 2003, **403**, 197–206.
40 R. P. Turcotte, J. O. Sawyer and L. Eyring, *Inorg. Chem.*, 1969, **8**, 238–246.

41 *CrystalMaker 9.0.3*, CrystalMaker Software Ltd, Oxford, England, 2014, https://www.crystalmaker.com.
42 J. Végh, *J. Electron Spectrosc. Relat. Phenom.*, 2006, **151**, 159–164.
43 R. W. M. Kwok, *XPSPEAK 4.1*, The Chinese University of Hong Kong, Hong Kong, 2000.
44 C. Anandan and P. Bera, *Appl. Surf. Sci.*, 2013, **283**, 297–303.
45 M. J. Frisch, G. W. Trucks, H. B. Schlegel, G. E. Scuseria, M. A. Robb, J. R. Cheeseman, G. Scalmani, V. Barone, G. A. Petersson, H. Nakatsuji, *et al.*, *Gaussian 09, Revision A.02*, Gaussian Inc., Wallingford CT, US, 2016.
46 A. D. Becke, *J. Chem. Phys.*, 1993, **98**, 5648–5652.
47 C. Lee, W. Yang and R. G. Parr, *Phys. Rev. B*, 1988, **37**, 785–789.
48 W. J. Stevens, H. Basch and M. Krauss, *J. Chem. Phys.*, 1984, **81**, 6026–6033.
49 W. J. Stevens, M. Krauss, H. Basch and P. G. Jasien, *Can. J. Chem.*, 1992, **70**, 612–630.
50 T. R. Cundari and W. J. Stevens, *J. Chem. Phys.*, 1993, **98**, 5555–5565.
51 T. Miyazaki, S. Okita, T. Ohta, H. Yagi, R. Sumii, H. Okimoto, Y. Ito, H. Shinohara and S. Hino, *Chem. Phys.*, 2015, **447**, 71–75.